arXiv:1207.0305v1 [quant-ph] 2 Jul 2012

Spatial and spectral properties of the pulsed second-harmonic generation in a PP-KTP waveguide

Radek Machulka[1,*], **Jiří Svozilík**[1,2], **Jan Soubusta**[3], **Jan Peřina, Jr.**[3], **and Ondřej Haderka**[1]

[1] *RCPTM, Joint Laboratory of Optics PU and IP AS CR, 17. listopadu 12, 771 46 Olomouc, Czech Republic*
[2] *ICFO—Institut de Ciencies Fotoniques, Mediterranean Technology Park, 08860, Castelldefels, Barcelona, Spain*
[3] *Institute of Physics of Academy of Science of the Czech Republic, Joint Laboratory of Optics of PU and IP AS CR, 17. listopadu 12, 772 07 Olomouc, Czech Republic*
[*] *radek.machulka@jointlab.upol.cz*

Abstract: Spatial and spectral properties of the pulsed second harmonic generation in a periodically-poled KTP waveguide exploiting simultaneously the first, second, and third harmonics of periodic nonlinear modulation are analyzed. Experimental results are interpreted using a model based on finite elements method. Correlations between spatial and spectral properties of the fundamental and second-harmonic fields are revealed. Individual nonlinear processes can be exploited combining spatial and spectral filtering. Also the influence of waveguide parameters to the second-harmonic spectra is addressed.

© 2012 Optical Society of America

OCIS codes: (230.7370) Waveguides; (190.2620) Harmonic generation and mixing; (230.4320) Nonlinear optical devices.

References and links

1. P.A. Franken, A.E Hill, C.W. Peters, and G. Weinreich, “Generation of optical harmonics,” Phys. Rev. Lett. **7**, 118 (1961).
2. A.S. Helmy, P. Abolghasem, J.S. Aitchison, B.J. Bijlani, J. Han, B.M. Holmes, D.C. Hutchings, U. Younis, and S.J. Wagner, “Recent advances in phase-matching second order nonlinearities in monolithic semiconductor waveguides,” Las. Phot. Rev. **5**, 272 (2011)
3. J.A. Armstrong, N. Bloembergen, J. Ducuing, and P.S. Pershan, “Interactions between light waves in a nonlinear dielectric,” Phys. Rev. **127**, 1918–1939 (1962).
4. M.M. Fejer, G.A. Magel, and E.J. Lim, “Quasi-phase-matched interactions in lithium niobate,” SPIE Proceedings on Nonlinear Optical Properties of Materials **1148**, SPIE, Washington, (1989).
5. M. Yamada, N. Nada, M. Saitoh, and K. Watanabe “First-order quasi-phase matched $LiNbO_3$ waveguide periodically poled by applying an external field for efficient blue second-harmonic generation,” Appl. Phys. Lett. **62**, 435 (1993).
6. M.M. Fejer, G.A. Magel, D.H. Jundt, and R.L. Byer, “Quasi-phase-matched second harmonic generation: tuning and tolerances,” IEEE J. Quantum Electron. **28**, 2631 (1992).
7. N.E. Yu, S. Kurimura and K. Kitamura, “ Higher-order quasi-phase matched second harmonic generation in periodically poled MgO-doped stoichiometric $LiTaO_3$,” J. Korean Phys.Soc. **47**, 636 (2005).
8. J. Chen, J.A. Pearlman, A. Ling, J. Fan, and L.A. Migdall, “A versatile waveguide source of photon pairs for chip-scale quantum information processing,” Opt. Express **17**, 6727–6740 (2009).
9. M.G. Roelofs, A. Suna, W. Bindloss, and J.D. Bierlein, “Characterization of optical waveguides in $KTiOPO_4$ by second harmonic spectroscopy,” J. Appl. Phys. **76**, 4999 (1994).
10. C.M. Kaleva, M. Munro, T.D. Roberts, T. Chang, and P. Battle, “Type II sum frequency generation in KTP waveguides: a technique for pre and post screening,” Proceedings of SPIE **6875**, 68751L (2008).

11. J. Peřina, “Quantum statistics of linear and nonlinear optical phenomena,” Kluwer, Dordrecht (1991).
12. J. Peřina Jr., O. Haderka, C. Sibilia, M. Bertolotti, and M. Scalora, “Squeezed-light generation in a photonic band-gap nonlinear planar waveguide,” Phys. Rev. A **76**, 033813 (2007).
13. M. Karpinski, C. Radzewicz, and K. Banaszek, “Experimental characterization of three-wave mixing in a multi-mode nonlinear KTiOPO$_4$ waveguide,” Appl. Phys. Lett. **94**, 181105 (2009).
14. A. Christ, K. Laiho, A. Eckstein, T. Lauckner, P.J. Mosley, and C. Silberhorn, “Spatial modes in waveguided parametric downconversion,” Phys. Rev. A **80**, 033829 (2009).
15. P.J. Mosley, A. Christ, A. Eckstein, and C. Silberhorn, “Direct measurement of the spatial-spectral structure of waveguided parametric down-conversion,” Phys. Rev. Lett. **103**, 233901 (2009).
16. K. Banaszek, A.B. U’Ren, and I.A. Walmsley, “Generation of correlated photons in controlled spatial modes by downconversion in nonlinear waveguides,” Opt. Lett. **26**, 1397–1369 (2001).
17. L. Mandel and E. Wolf, “Optical coherence and quantum optics,” Cambridge Univ. Press, (1995).
18. R. Boyd, “Nonlinear optics, third edition,” Elsevier, Amsterdam (2008).
19. A.W. Snyder and J. Love, “Optical waveguide theory,” Springer, (1983).
20. T.Y. Fan, C.E. Huang, B.Q. Hu, C. Eckardt, Y.X. Fan, R.L. Byer, and R.S. Feigelson, “SHG and accurate index of refraction measurements in flux-grown KTiOPO$_4$,” Appl. Opt. **26**, 2390–2394 (1987).
21. J.D. Bierlein, A. Ferretti, L.H. Brixner, and W.Y. Hsu, “Fabrication and characterization of optical waveguides in KTiOPO$_4$,” Appl. Phys. Lett. **50**, 1216-1218 (1987).
22. E. Kawano and T. Kitoh, “Introduction to optical waveguide analysis: solving Maxwell’s equation and the Schrodinger equation,” Wiley, (2001).
23. I. Rubinstein and L. Rubinstein, “Partial differential equations in classical mathematical physics,” Cambridge University Press, (1998).
24. M. Fiorentino, S.M. Spillane, R.G. Beausoleil, T.D. Roberts, P. Battle, and M.W. Munro, “Spontaneous parametric down-conversion in periodically poled KTP waveguides and bulk crystals,” Opt. Express **15**, 7479–7488 (2007).
25. A.B. Fallahkhair, K.S. Li, and T.E. Murphy, “Vector finite difference modesolver for anisotropic dielectric waveguides,” J. Lightwave Technol. **26**, 1423–1431 (2008).
26. J. Jin, “The finite element method in electromagnetics, 2nd edition,” Wiley, (2002).
27. S.M. Spillane, M. Fiorentino, and R.G. Beausoleil, “Spontaneous parametric down conversion in a nanophotonic waveguide,” Opt. Express **15**, 8770–8780 (2007).
28. C. Kaleva, private communication, (February 2012).
29. N.E. Yu, J.H. Ro, H.K. Kim, M. Cha, I. Hanaka, K. Nakamura and H. Ito, “High order quasi-phase-matched second harmonic generations in periodically poled lithium niobate,” J. Korean Phys. Soc. **35**, 1384 (1999).
30. J. Peřina Jr., “Quantum properties of counter-propagating two-photon states generated in a planar waveguide,” Phys. Rev. A **77**, 013803 (2008).
31. Z.H. Levine, J. Fan, J. Chen, A. Ling, and A. Migdall “Heralded, pure-state single-photon source based on a potassium titanyl phosphate waveguide,” Opt. Express **18**, 3708–3718 (2010).
32. M.F. Saleh, B.E Saleh, and M.C. Teich “Modal, spectral, and polarization entanglement in guided-wave parametric down-conversion,” Phys. Rev. A **79**, 053842 (2009).

---

1. Introduction

The process of second harmonic generation (SHG) has been one of the most frequently studied nonlinear optical phenomena since the invention of lasers. This process was observed by Franken et al. in 1961 for the first time using crystalline quartz [1]. In principle, a second-harmonic (SH) field can be generated in many nonlinear materials that lack the inversion symmetry. However, phase matching of the nonlinearly interacting fields cannot be reached provided that the normal dispersion occurs [2]. Here, nonlinear anisotropic crystals with their birefringence have been found useful and allowed to fulfil phase-matching conditions.

Alternatively, nonzero phase mismatch $\Delta\mathbf{k}$ among the interacting fields can be compensated by a periodic spatial modulation of the nonlinear susceptibility with period $\Lambda_{\rm PM}$ ($\Lambda_{\rm PM} = 2\pi/|\Delta\mathbf{k}|$), as has been suggested by Armstrong [3]. A commonly used technique in this case is based on inverting dielectric domains inside a ferro-electric nonlinear crystal using an intense static electric field [4, 5]. This process is called periodic poling (PP) and has allowed to utilize the highest material nonlinear coefficients [6].

The poling process leaves well defined domains of the alternating sings inside the nonlinear material. $\chi^{(2)}$ nonlinearity can thus be approximated by a dichotomic function that can have significant coefficients at its first- as well as higher-order harmonics. Usually, a nonlinear structure is designed such that only one harmonic is exploited. Contributions from other harmonics are considered as parasitic [7] in this case. If domain lengths are chosen such that several harmonics of nonlinear modulation are significant a rich spatial and spectral modal structure in a waveguide can be exploited [8]. This gives a substantial increase in the ability to tailor properties of the nonlinear process inside a waveguide. Here, we study these abilities considering a waveguide that uses the first three harmonics of nonlinear modulation.

Efficiency of the SHG process is inversely proportional to the transverse area of the fundamental beam and, as a consequence, beam focusing may improve the efficiency of SHG. However, walk-off of the interacting fields puts limits to this property in bulk crystals. For this reason, waveguiding structures not suffering from this problem have become very important [9]. They have allowed to confine fields' energies into a very small area (typically of the order of tens of μm^2) that results in the desirable high power densities [10]. Intense SH fields can then be obtained which, among others, allow to generate squeezed light [11, 12].

Usually, waveguides support the propagation of the fundamental as well as several higher-order modes, for which intensity oscillations in the transverse plane are typical. The guided modes differ in their wave vectors (propagation constants). The phase-matching conditions and efficient SHG process can be reached simultaneously for several combinations of these spatial modes [13, 14, 15]. For each of these individual phase-matched processes, certain spectral and also spatial characteristics of the fundamental beam are needed. We note that as we are interested in pulsed SHG we consider spectrally polychromanic modes determined by phase-matching conditions for spatially defined modes. Different spectral properties for different individual processes are useful in tuning a specific nonlinear process. We note that, on the top of phase-matching conditions, also a sufficient spatial overlap of electric-field amplitudes of the interacting guided modes is needed. This disqualifies higher-order modes whose amplitudes change their signs several times in the transverse plane. Precise determination of efficient combinations of the modes is thus very important in characterizing the analyzed waveguide. This characterization is useful not only for the SHG process. Also the inverse process of spontaneous parametric down-conversion well known for its ability to generate entangled photon pairs [14, 15, 16] benefits from the analysis.

Waveguides are promising not only as efficient media for nonlinear interactions, they also allow for miniaturization and integration into more complex circuits. Their nonlinearities allow for the generation of squeezed light that is useful for optical communications and quantum metrology [17].

The theory of SHG in periodically poled waveguides is introduced in Sec. 2. Equations giving the transverse profiles of the fundamental and SH modes are derived in Sec. 3. The calculated and measured SH spectra are analyzed in Sec. 4. Spectral and spatial properties of type II SHG are discussed in Sec. 5. Conclusions are drawn in Sec. 6.

2. Second-harmonic generation

The evolution of electric-field amplitude $\mathbf{E}^{(2)}$ of the SH field inside the waveguide is governed by the nonlinear wave equation [17, 18]:

$$\nabla \times \left(\nabla \times \mathbf{E}^{(2)} \right) + \frac{\overleftrightarrow{\varepsilon}}{c^2} \frac{\partial^2 \mathbf{E}^{(2)}}{\partial t^2} = -\mu_0 \frac{\partial^2 \mathbf{P}^{(2)}}{\partial t^2}; \tag{1}$$

$\nabla = \mathbf{x}\frac{\partial}{\partial x} + \mathbf{y}\frac{\partial}{\partial y} + \mathbf{z}\frac{\partial}{\partial z}$. Linear permittivity tensor $\overleftrightarrow{\varepsilon}$ is assumed to have a diagonal form in the used cartesian coordinate system $\{x, y, z\}$. Constant c means speed of light in vacuum and μ_0 is vacuum permeability. Vector $\mathbf{P}^{(2)}$ of the second-order polarization introduced in Eq. (1) can be expressed as $\mathbf{P}^{(2)} = 2\varepsilon_0 \overleftrightarrow{d} : \mathbf{E}^{(1)}\mathbf{E}^{(1)}$, where $\overleftrightarrow{d}$ is the third-order tensor of nonlinear coefficients and $\mathbf{E}^{(1)}$ denotes an electric-field amplitude of the fundamental pumping field. Symbol : stands for tensor shortening with respect to its indices.

The electric field amplitudes of both the fundamental [$\mathbf{E}^{(1)}$] and SH [$\mathbf{E}^{(2)}$] fields can be spectrally decomposed as follows:

$$\mathbf{E}^{(j)}(x,y,z,t) = \sum_{p=\mathrm{TE,TM}} \sum_{n} \int d\omega \mathscr{E}_{pn}^{(j)}(z,\omega)\mathbf{e}_{pn}^{(j)}(x,y,\omega) \exp\left[i\beta_{pn}^{(j)}(\omega)z - i\omega t\right], \quad j = 1,2. \quad (2)$$

The normalized electric-field mode functions $\mathbf{e}_{pn}^{(j)}(x,y,\omega)$ form a basis and are obtained as eigenfunctions of the Helmholtz equation (see later in Sec. 3). The Helmholtz equation also provides the corresponding propagation constants $\beta_{pn}^{(j)}(\omega)$. A detailed analysis of modal properties of the studied waveguide has shown that two groups of modes differing in polarization exist [19]. Whereas (quasi-) TE modes have electric-field polarization vectors nearly parallel to the x axis, electric-field polarization vectors of (quasi-) TM modes are nearly perpendicular to the x axis. In addition, there exists a system of transverse modes labelled by index n. Finally, envelopes $\mathscr{E}_{pn}^{(j)}(z,\omega)$ of the spectral amplitudes of the corresponding modes propagating along the $+z$ axis have been introduced in Eq. (2).

Substituting the decomposition of electric-field amplitudes $\mathbf{E}^{(j)}$ in Eq. (2) into the wave equation (1) a set of nonlinear differential equations for the envelope amplitudes $\mathscr{E}_{pn}^{(j)}(z,\omega)$ can be derived. Invoking the slowly varying amplitude approximation and non-depleted fundamental pump field approximation, the following formula for envelope amplitude $\mathscr{E}_{ak}^{(2)}$ at the end of the waveguide of length L has been obtained after simple integration:

$$\begin{aligned}\mathscr{E}_{ak}^{(2)}(L,\omega_2) \quad = \quad & \frac{i\omega_2^2}{c^2\left[\beta_{ak}^{(2)}(\omega_2)\right]^2} \sum_{b,c=\mathrm{TE,TM}} \sum_{l,m} \int d\omega_1 D_{klm}^{abc}(\omega_2,\omega_1)\Gamma_{klm}^{abc}(L,\omega_2,\omega_1) \\ & \times \mathscr{E}_{bl}^{(1)}(0,\omega_1)\mathscr{E}_{cm}^{(1)}(0,\omega_2-\omega_1). \end{aligned} \quad (3)$$

We note that the integration over frequency ω_1 incorporates all frequency contributions occurring in the polychromatic fundamental field. In Eq. (3), effective nonlinear coefficients D_{klm}^{abc} have been introduced:

$$D_{klm}^{abc}(\omega_2,\omega_1) = d_M \int_{-\infty}^{\infty} dx \int_{-\infty}^{\infty} dy \overleftrightarrow{d} : \mathbf{e}_{ak}^{(2)*}(x,y,\omega_2)\mathbf{e}_{bl}^{(1)}(x,y,\omega_1)\mathbf{e}_{cm}^{(1)}(x,y,\omega_2-\omega_1). \quad (4)$$

The effective nonlinear coefficients D_{klm}^{abc} incorporate in their definitions both polarization properties and overlap of the transverse parts of the interacting modes amplitudes. Constant d_M gives the amplitude of decomposition of the actual modulation of nonlinear coefficient into the M-th harmonic. The coefficients D_{klm}^{abc} are assumed to be weakly frequency dependent. Considering nonlinear coefficients D_{klm}^{abc} involving higher-order spatial modes, their values are usually small due to frequent changes in the sign of the electric-field amplitudes of these modes in the transverse plane. The coupling functions $\Gamma_{klm}^{abc}(L,\omega_2,\omega_1)$ introduced in Eq. (3) characterize fields' evolution along the z axis:

$$\Gamma_{klm}^{abc}(L,\omega_2,\omega_1) = i\frac{\exp\left[-i\Delta\beta_{klm}^{abc}(\omega_2,\omega_1)L\right]-1}{\Delta\beta_{klm}^{abc}(\omega_2,\omega_1)}. \quad (5)$$

The nonlinear phase mismatch $\Delta\beta_{klm}^{abc}$ occurring in Eq. (5) is defined as

$$\Delta\beta_{klm}^{abc}(\omega_2,\omega_1) = \beta_{ak}^{(2)}(\omega_2) - \beta_{bl}^{(1)}(\omega_1) - \beta_{cm}^{(1)}(\omega_2-\omega_1) - \frac{2\pi M}{\Lambda_{\mathrm{PM}}}; \quad (6)$$

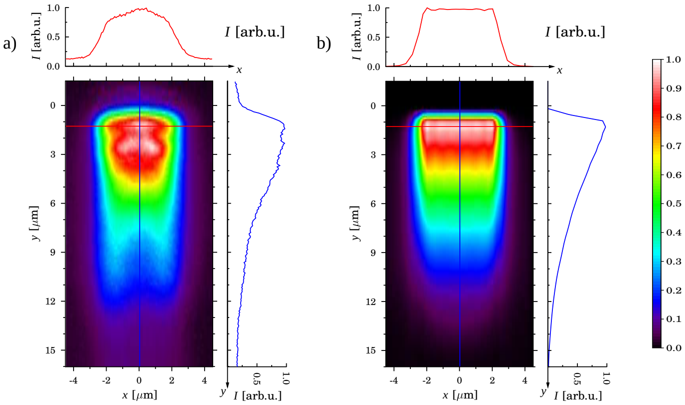

Fig. 1. Topo graphs of (a) experimental and (b) theoretical intensity $I = |\mathscr{E}^{(1)}|^2$ in the transverse plane formed by white light propagating inside the waveguide. Also cuts along the lines indicated in the topo graphs are shown.

the last contribution $2\pi M/\Lambda_{\rm PM}$ originates in the M-th harmonic of the periodic modulation of nonlinear coefficient.

3. Equations giving fields' spatial profiles

Material of the waveguide, KTP, is anisotropic and is positioned such that only diagonal elements ε_x, ε_y, and ε_z of the linear susceptibility tensor are nonzero. The crystallographic axes of KTP (x_c, y_c, z_c) coincide with the axes of the coordinate system (z, x, y). The elements ε_x, ε_y, and ε_z can be expressed using indices of refraction n_ξ ($\varepsilon_\xi = n_\xi^2$), $\xi = x,y,z$, that take the following form in the studied waveguide [9, 20, 21]:

$$\begin{aligned} n_\xi(x,y)\Big|_{y\geq 0} &= n_{\xi 0} + \Delta n_\xi \,\mathrm{rect}_{[-w/2,w/2]}(x)\,\mathrm{erfc}\,(-y/h)\,, \\ n_\xi(x,y)\Big|_{y<0} &= 1; \qquad\qquad \xi = x,y,z. \end{aligned} \tag{7}$$

The indices of refraction $n_{\xi 0}$ characterize the substrate. Changes Δn_ξ of the indices of refraction are introduced in the process of waveguide formation. For λ_1 = 800 nm (λ_2 = 400 nm) the following values have been used: $n_x = 1.75719$, $\Delta n_x = 0.009$, $n_y = 1.84546$, $\Delta n_y = 0.013$ ($n_x = 1.84435$, $\Delta n_x = 0.018$, $n_y = 1.96775$, $\Delta n_y = 0.019$) [20]. Above the waveguide, air is assumed. Waveguide's depth is characterized by parameter h, whereas parameter w denotes waveguide's width. We have assumed $h = 10$ μm and $w = 5$ μm for the analyzed waveguide. These values have been checked experimentally by measuring the profile of white light leaving the waveguide and comparing the obtained profile with that arising from the model (see Fig. 1). The rectangular function $\mathrm{rect}_{[-w/2,w/2]}(x)$ equals 1 in the interval $\langle -w/2, w/2\rangle$ and is zero otherwise. Also the error function $\mathrm{erfc}(x)$ has been invoked in Eq. (7).

Usually, TE modes are conveniently obtained by solving the wave equation for the electric-field amplitude. The wave equation for the magnetic-field amplitude is then useful in determining TM modes. However, the spatial dependence of indices of refraction in the studied waveguide causes difficulties and asymmetry in the obtained equations. As a consequence, the use of wave equation for the magnetic-field amplitude $\mathbf{H}$,

$$\nabla \times \left(\overleftrightarrow{\varepsilon}^{-1} \nabla \times \mathbf{H} \right) = -\frac{1}{c^2}\frac{\partial^2 \mathbf{H}}{\partial t^2}, \tag{8}$$

is preferred in both cases.

The substitution $\mathbf{H}(x,y,z,t) = \mathbf{h}(x,y,\omega)\exp(i\beta z - i\omega t)$ in Eq. (8) provides a set of equations for cartesian components of the magnetic-field envelope $\mathbf{h}(x,y,\omega)$ of a mode characterized by frequency ω and propagation constant β. Considering the relation

$$\mathbf{h}_z = i(\partial\mathbf{h}_x/\partial x + \partial\mathbf{h}_y/\partial y)/\beta \tag{9}$$

originating in the Maxwell equation $\nabla\mathbf{H} = 0$, two coupled differential equations for the components $\mathbf{h}_x$ and $\mathbf{h}_y$ can be derived:

$$\frac{1}{\varepsilon_y}\frac{\partial^2\mathbf{h}_x}{\partial x^2} + \frac{1}{\varepsilon_z}\frac{\partial^2\mathbf{h}_x}{\partial y^2} + \frac{1}{\varepsilon_y}\frac{\partial^2\mathbf{h}_y}{\partial x\partial y} - \frac{1}{\varepsilon_z}\frac{\partial^2\mathbf{h}_y}{\partial y\partial x} - \left[\frac{\partial\mathbf{h}_y}{\partial x} - \frac{\partial\mathbf{h}_x}{\partial y}\right]\frac{\partial}{\partial y}\left(\frac{1}{\varepsilon_z}\right) = \left(\frac{\beta^2}{\varepsilon_y} - k_0^2\right)\mathbf{h}_x, \tag{10}$$

$$\frac{1}{\varepsilon_z}\frac{\partial^2\mathbf{h}_y}{\partial x^2} + \frac{1}{\varepsilon_x}\frac{\partial^2\mathbf{h}_y}{\partial y^2} + \frac{1}{\varepsilon_x}\frac{\partial^2\mathbf{h}_x}{\partial y\partial x} - \frac{1}{\varepsilon_z}\frac{\partial^2\mathbf{h}_x}{\partial x\partial y} + \left[\frac{\partial\mathbf{h}_y}{\partial x} - \frac{\partial\mathbf{h}_x}{\partial y}\right]\frac{\partial}{\partial x}\left(\frac{1}{\varepsilon_z}\right) = \left(\frac{\beta^2}{\varepsilon_x} - k_0^2\right)\mathbf{h}_y, \tag{11}$$

$k_0 = \omega/c$. The last component $\mathbf{h}_z(x,y,\omega)$ is then obtained from Eq. (9) provided that the remaining components have been determined. Knowing the magnetic-field envelope $\mathbf{h}$, the electric-field envelope $\mathbf{e}$ is derived from the Maxwell equation that gives $\mathbf{e}(x,y,\omega) = \overleftrightarrow{\varepsilon}^{-1}[i\nabla\times\mathbf{h}(x,y,\omega) - \beta\mathbf{z}\times\mathbf{h}(x,y,\omega)]/(\varepsilon_0\omega)$; $\mathbf{z}$ means the unit vector along the z axis.

Considering Eqs. (10) and (11), the cross contributions

$$\begin{array}{lll} \dfrac{1}{\varepsilon_y}\dfrac{\partial^2\mathbf{h}_y}{\partial x\partial y}, & \dfrac{1}{\varepsilon_z}\dfrac{\partial^2\mathbf{h}_y}{\partial y\partial x}, & \left[\dfrac{\partial\mathbf{h}_y}{\partial x} - \dfrac{\partial\mathbf{h}_x}{\partial y}\right]\dfrac{\partial}{\partial y}\left(\dfrac{1}{\varepsilon_z}\right), \\ \dfrac{1}{\varepsilon_x}\dfrac{\partial^2\mathbf{h}_x}{\partial y\partial x}, & \dfrac{1}{\varepsilon_z}\dfrac{\partial^2\mathbf{h}_x}{\partial x\partial y}, & \left[\dfrac{\partial\mathbf{h}_y}{\partial x} - \dfrac{\partial\mathbf{h}_x}{\partial y}\right]\dfrac{\partial}{\partial x}\left(\dfrac{1}{\varepsilon_z}\right) \end{array}$$

are usually very small and so they can be omitted [22]. As a result, equations (10) and (11) become independent and so can be solved separately giving (quasi-) TE and TM modes. This considerably simplifies the analysis. The obtained equations can be written as follows:

$$\begin{aligned} \frac{\partial^2\mathbf{h}_x}{\partial x^2} + \frac{\varepsilon_y}{\varepsilon_z}\frac{\partial^2\mathbf{h}_x}{\partial y^2} &= \left(\beta^2 - \varepsilon_y k_0^2\right)\mathbf{h}_x, \\ \frac{\varepsilon_x}{\varepsilon_z}\frac{\partial^2\mathbf{h}_y}{\partial x^2} + \frac{\partial^2\mathbf{h}_y}{\partial y^2} &= \left(\beta^2 - \varepsilon_x k_0^2\right)\mathbf{h}_y. \end{aligned} \tag{12}$$

For certain profiles of permittivity $\overleftrightarrow{\varepsilon}$, the solution of Eqs. (12) can be found analytically [19, 23]. For example, the simplest approximation of waveguide's profile by the rectangular functions in both x and y directions together with the known analytical form of eigenmodes has been used in [14] to interpret the experimental results. However, only the numerical approach is possible for transverse profiles of real waveguides. For this reason, a large variety of sophisticated numerical methods has been developed [22]. Among them, a finite difference method has become popular because of simple implementation, even in its full-vector form. Unfortunately, it requires a large amount of computer resources for solving the eigenvalue problem. This represents a problem when more complex transverse profiles are considered. Nevertheless, it has been successfully applied both in its scalar [24] as well as semi-vectorial [13, 25] forms.

On the other hand, a finite elements method [22, 26] has been found more suitable due to its stability and lower demands on computer resources. It is resistant against non-physical solutions. Moreover, the use of higher-order approximation functions results in lowering of the dimension of eigenvalue problem. For this reason, many commercial waveguide mode-solvers are based upon this method. For instance, it has been applied for the determination of waveguide's mode dispersion in [27]. In our investigation, we have developed an implementation of

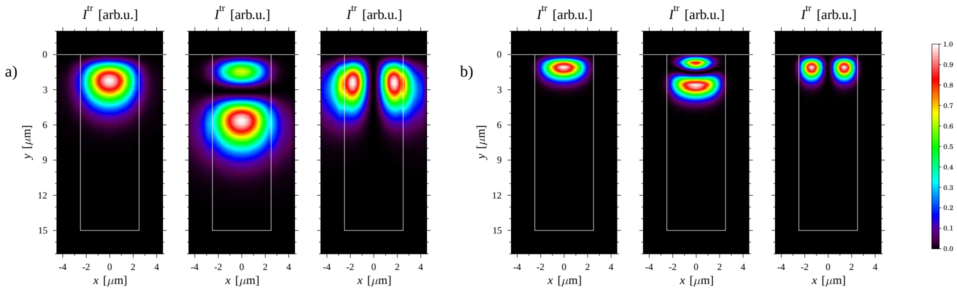

Fig. 2. Topo graphs of calculated electric-field intensity distributions I^{tr} ($I^{\text{tr}}(x,y) = |\mathbf{e}(x,y)|^2$) in the transverse plane for the first three spatial modes denoted as (0,0), (0,1), and (1,0) for the fundamental TE-polarized (a) and SH TE-polarized (b) field; $w = 5$ μm, $h = 10$ μm. Frame boxes in the graphs indicate boundaries of the waveguide.

the finite elements method that is based on the Galerkin method [22]. Easy parallelization of this implementation makes it superior above other approaches.

Intensity profiles of the first three modes both for the fundamental and SH TE-polarized fields as they emerge from the developed method are depicted in Fig. 2. The transverse profiles of TM-polarized modes are similar to those appropriate to the corresponding TE-polarized modes. According to the convention, spatial modes are labelled by two numbers that give the number of nodes along the x and y axes. The numerical analysis has revealed that the analyzed waveguide supports more than 30 spatial modes at $\lambda_2 = 400$ nm for both TE and TM polarizations and 3 (5) spatial modes at $\lambda_1 = 800$ nm for TE (TM) polarization.

4. Experimental second harmonic generation in the waveguide

The analyzed waveguide was fabricated on a KTP substrate ($10.5 \times 2 \times 1$ mm^3) by Rb$^+$ ion diffusion together with other cca 50 similar waveguides (manufacturer AdvR Inc.). The requirement for an efficient type II SHG at $\lambda_1 = 800$ nm has resulted in poling the nonlinear material with period $\Lambda_{\text{PM}} = 7.62$ μm. In the fabrication process both horizontal and vertical dimensions of the waveguide are under control. The horizontal width is given by geometry of the lithographic mask that leads to a profile with well defined boundaries owing to highly anisotropic diffusion. On the other hand, the profile in the vertical direction is formed by ion diffusion gradually in time. At some instant the profile of refractive index becomes temporally stable and can be approximated by the error function [21].

Due to imperfections in the fabrication process, fluctuations in waveguide's parameters including its width w, depth h, duty ratio of the poling period as well as the poling period itself inevitably occur. Moreover, there exist several areas without poling inside the structure and also the poling duty ratio may change from 50 % to 75 %. These fluctuations result in broadening of the SH spectrum. To judge the amount of spectral broadening we have plotted the dependence of SH wavelength shift $\Delta\lambda_2$ on waveguide's width w, depth h and poling period Λ_{PM} in Fig. 3 for five individual nonlinear processes dominating in SH spectrum. According to the manufacturer [28], the expected variations in waveguide's width w, depth h and poling period Λ_{PM} are in turn ± 0.1 μm, ± 2 μm and ± 0.1 μm. This in accord with the curves of Fig. 3 results in the estimated spectral SH widths equal approximately to 0.05 nm, 0.1 nm, and 2 nm, respectively. Fluctuations in the poling period Λ_{PM} thus represent the main source of SH spectral broadening observed with a sufficiently broad fundamental spectrum. Imperfections in nonlinear modulation even lead to the occurrence of three SH fields originating in different polarization configurations and having different ideal values of poling period Λ_{PM} (see below).

Larger differences in the values of width w, depth h and poling period Λ_{PM} lead to significant shifts of spectral positions of individual lines that result in the change of the overall SH spectral profile. The character of this change is illustrated in Fig. 4 showing the calculated SH intensity spectrum I for three values of the width w.

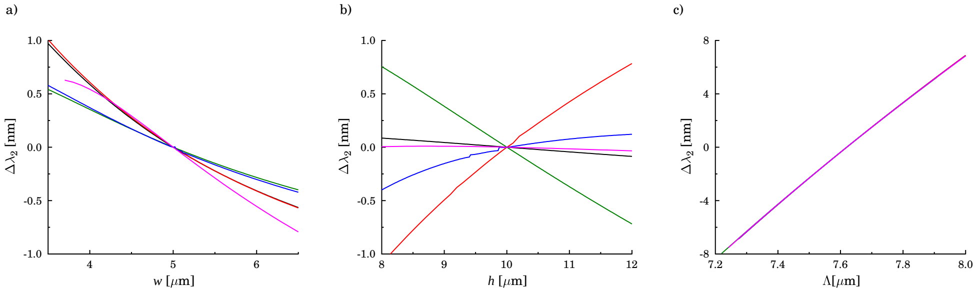

Fig. 3. SH wavelength shift $\Delta\lambda_2$ as it depends on waveguide's width w (a), depth h (b) and poling period Λ_{PM} (c) for the following individual processes: (0,0) + (0,0) $\rightarrow$ (0,0) (black curve), (0,0) + (0,0) $\rightarrow$ (0,1) (red curve), (0,1) + (0,1) $\rightarrow$ (0,0) (green curve), (0,1) + (0,1) $\rightarrow$ (0,1) (blue curve), and (1,0) + (0,0) $\rightarrow$ (1,0) (magenta curve). In (c), all curves nearly coincide.

To observe the full profile of a spectral line characterized by its width $\Delta\lambda_2$, the width $\Delta\lambda_1$ of the fundamental field has to be sufficiently large. Consideration of energy conservation in the nonlinear process provides in this case the relation $\Delta\lambda_1 = 2\sqrt{2}\Delta\lambda_2$. However, the needed width $\Delta\lambda_1$ has to be larger than $2\sqrt{2}\Delta\lambda_2$ because of phase-matching conditions that put additional constraints to the nonlinear process. This relation between the widths $\Delta\lambda_1$ and $\Delta\lambda_2$ also determines how wide area in the SH spectrum is observed for a given fundamental spectral width $\Delta\lambda_1$. We note that a more detailed information about the phase-matching conditions and their spectral dependence inside a broadened line can be reached by sum-frequency generation utilizing spectrally narrow fields [13].

The experimental investigation of SHG process has been carried out in the setup sketched

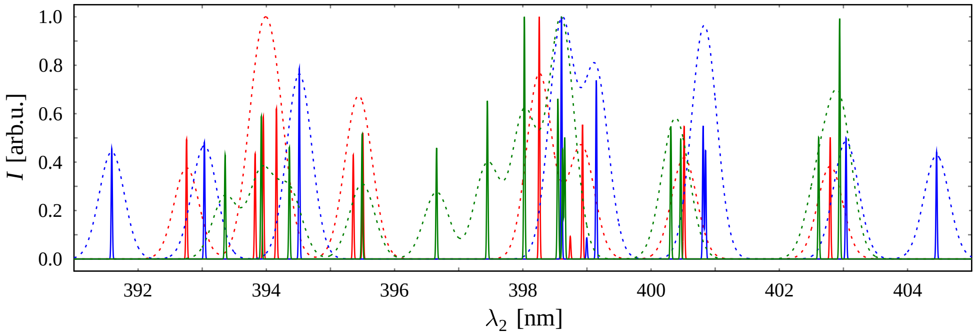

Fig. 4. SH spectral intensity I depending on wavelength λ_2 and calculated for different values of waveguide's width w; $I(\omega_2) = \sum_{ak} |\mathscr{E}_{ak}(L,\omega_2)|^2$. Solid curves correspond to ideal spectral resolution 0.13 nm (given by phase-matching conditions along the z axis for a 10.5 mm long waveguide with the inclusion of material and waveguiding dispersion). Dashed curves are appropriate for the expected real spectral broadening of 1 nm; $w = 4$ μm (blue curve), $w = 5$ μm (red curve) and $w = 6$ μm (green curve), $h = 10$ μm.

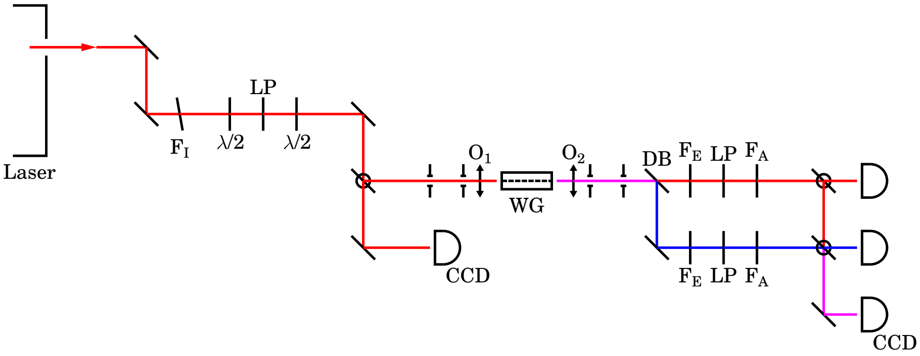

Fig. 5. Sketch of the experimental setup for waveguide (WG) investigation. Symbol F_I denotes interference filter, F_A neutral density filter, F_E edge-pass filter, $\lambda/2$ half-wave plate, LP linear polarizer, O microscope objective, DB dichroic beam-splitter, and CCD means CCD camera.

in Fig. 5. Light from a tunable femtosecond Ti-sapphire laser (87 MHz repetition rate, 100 fs pulse duration, central wavelengths in the range 790—810 nm, spectral width 10 nm) has been attenuated combining half-wave plate ($\lambda/2$) and linear polarizer to attain the power of about 20 mW. Another half-wave plate ($\lambda/2$) has been used to control the pump-beam polarization. The pump-beam central wavelength has been adjusted by tilting an interference filter defining the spectral width of 3 nm. A small fraction of the beam has been deflected to allow for precise monitoring of the pump-beam position in the transverse plane needed for efficient coupling of the beam into the waveguide using a 10× microscope objective. The light leaving the waveguide and composed of both the pump and SH beams has been imaged by a 20× objective with a larger numerical aperture. A dichroic beam-splitter has separated the pump beam from the SH beam. The obtained beams have been analyzed by power-meter, CCD camera or spectrometer (resolution 0.1 nm) after passing through a linear polarizer. As the indices of refraction in KTP are temperature dependent, the KTP chip has been thermally stabilized at 25 °C using a Peltier element with temperature sensor and feedback loop. We note that the ideal phase-matching condition shifts by cca 1 nm per 25 °C.

For the chosen orientation of KTP, three types of SHG processes differing in fields' polarization properties can occur simultaneously due to different harmonics of the periodical modulation of nonlinearity. In type 0 SHG, both the fundamental and SH fields have TM polarizations. If the fundamental beam is TE polarized and the SH beam TM polarized type I SHG is observed. A TE-polarized SH beam occurs only if both TE- and TM-polarized components of the fundamental beam are present (type II SHG). Different conversion efficiencies are found for the discussed processes because of different values of used nonlinear coefficients, overlaps of mode functions, and also phase-matching conditions. Especially, phase-matching conditions depending on the value of poling period Λ_{PM} allow to control these efficiencies. The analyzed waveguide was primarily optimized for type II SHG giving $\Lambda_{PM} = 7.62\ \mu$m. Nevertheless, type 0 SHG (with the optimum poling period 3.08 μm) can be observed exploiting the second harmonic of nonlinear periodic modulation. The presence of second harmonic of nonlinear periodic modulation together with all even harmonics is caused by the declination of the actual nonlinear modulation from the ideal shape with positive and negative domains of equal lengths [29]. We note that a nonlinear modulation with equal lengths of positive and negative domains has only odd harmonics nonzero. Also, the third harmonic of nonlinear periodic modulation allows to approximately arrive at the phase-matching conditions of type I SHG for which the

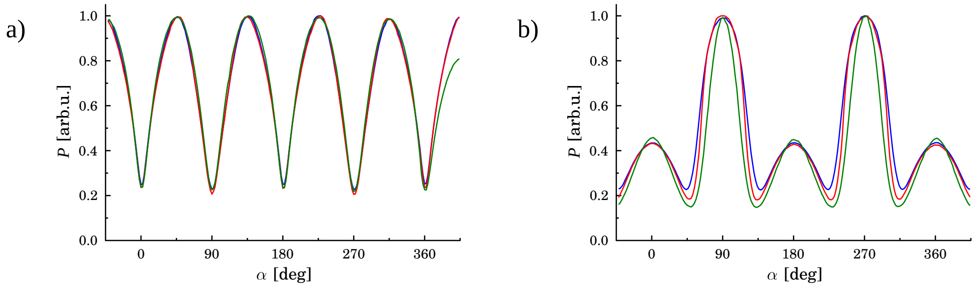

Fig. 6. Measured normalized power P of SH field as it depends on angle α giving the orientation of linear polarization of the incident pump beam for (a) TE- and (b) TM-polarized SH field ($\alpha = 0$ deg corresponds to TE polarization). Curves characterizing three different waveguides are shown for comparison to judge fabrication capabilities. The curves were obtained with experimental relative error 4 %.

poling period 1.83 μm would have been optimum. The experimental nonlinear conversion efficiencies η in this configuration are summarized in Tab. 1. Type II SHG is the most efficient process due to optimum phase-matching conditions and despite the lower value of nonlinear coefficient d_{32} compared to that of coefficient d_{33} used in type 0 SHG. Also better phase-matching conditions of type I SHG allow more efficient SHG than in type 0. However, and importantly, all three types of SHG have comparable efficiencies. Their relative values can suitably be changed by changing the poling period Λ_{PM}.

	Process	d [pm·V^{-1}]	η [W^{-1}·cm^{-2}]
type 0	TM + TM → TM	d_{33} = 10.7	2.83 ± 0.06
type I	TE + TE → TM	d_{32} = 2.65	4.44 ± 0.12
type II	TE + TM → TE	d_{32} = 2.65	4.78 ± 0.03

Table 1. Types of observed SHG processes, their polarizations, used nonlinear coefficients d [18], and experimental nonlinear conversion efficiencies η are given. Conversion efficiency η has been determined as $\eta = P_{\mathrm{SHG}} P_{\mathrm{in}}^{-2} L^{-2}$, where P_{SHG} (P_{in}) gives the power of outgoing SH (coupled incident pump) beam and L is the length of nonlinear medium [10].

Suitable choice of polarization directions of both the fundamental and SH fields allows to extract individual types of SHG. The intensity of SH field in the most efficient type II SHG process can be separated from the overall field by using a polarization analyzer aligned along TE polarization. The experimental evidence of observing this process is given by measuring periodic oscillations of SH intensity depending on the orientation of linear polarization of the incident pump beam [see Fig. 6(a)]. Aligning the polarization analyzer in SH field along TM polarization the remaining two processes are visible. Changing the orientation of linear polarization of the incident pump beam, we continuously move from one process to the other [see Fig. 6(b)]. Whereas TM polarization of the pump beam supports type 0 SHG, TE polarization is suitable for type I SHG.

We further pay attention to the most efficient type II SHG process. The necessity to have both TE- and TM-polarized fundamental field distinguishes it from the remaining two types. This is important from the point of view of the reverse process of parametric down-conversion [14, 15, 17, 30, 31] in which pairs of photons with orthogonal polarizations are emitted. The

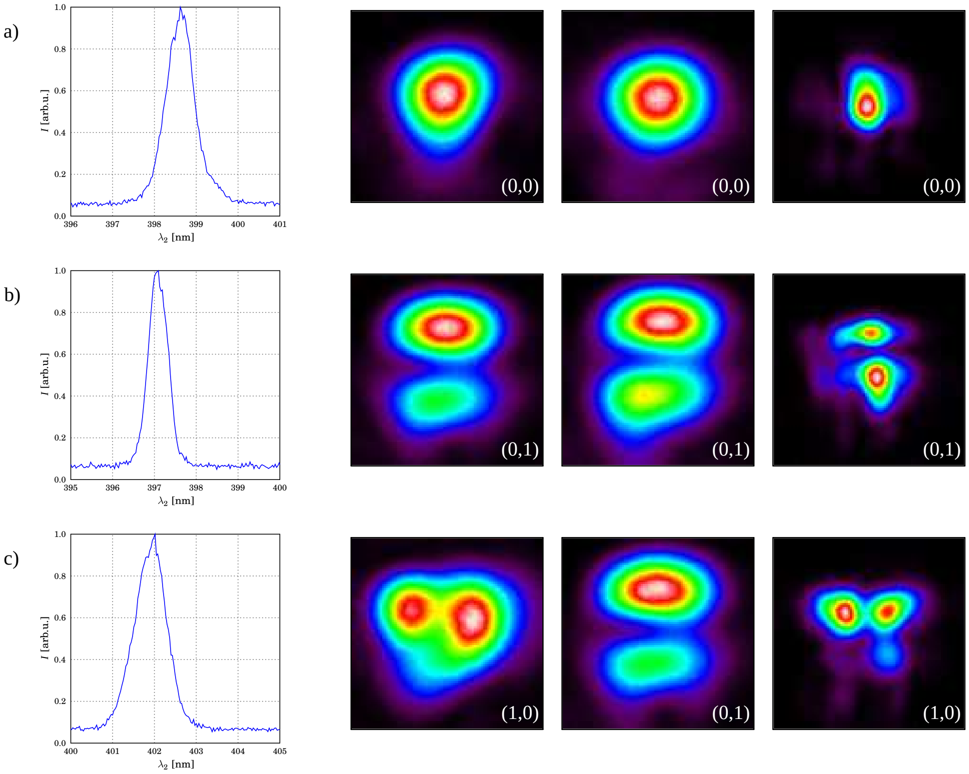

Fig. 7. Experimental SH spectral intensity I depending on wavelength λ_2 and topo graphs of spatial electric-field intensity profiles $I^{\mathrm{tr}}(x,y)$ of TE-polarized pump beam, TM-polarized pump beam, and TE-polarized SH beam are shown in sequence for individual processes: (a) (0,0) + (0,0) → (0,0), (b) (0,1) + (0,1) → (0,1), and (c) (1,0) + (0,1) → (1,0).

orthogonal polarizations of two photons would then allow to spatially separate both photons using a polarizing beam-splitter.

5. Spatial and spectral properties of type II second harmonic generation

In agreement with the numerical analysis, the experiment has revealed three (five) spatial TE- (TM-) polarized modes [(0,0), (0,1), (1,0), (1,1), and (0,2)] in the fundamental field inside the waveguide (see Fig. 7). As expected, the spatial modal structure of the SH field has been found richer owing to doubled relative waveguide dimensions with respect to the SH wavelength. The experimental spatial intensity profiles shown in Fig. 7 are partially distorted in comparison with the theoretical ones. This is caused by waveguide imperfections, non-ideal coupling of the fundamental beam leading to the excitation of more than one spatial mode and subsequent SHG into several spatial modes.

In the nonlinear process, a sufficient overlap of three chosen spatial mode profiles is needed to observe an individual nonlinear process in the measured SH spectrum. As also phase-matching conditions play an important role, a given individual process occurs only in a restricted spectral range of SH field (see Fig. 7). If spatial modes of the fundamental field are uniformly excited by a spectrally broad pumping, several individual nonlinear processes typically occur in the waveguide and contribute to the SH spectrum. As a consequence, the expected SH intensity

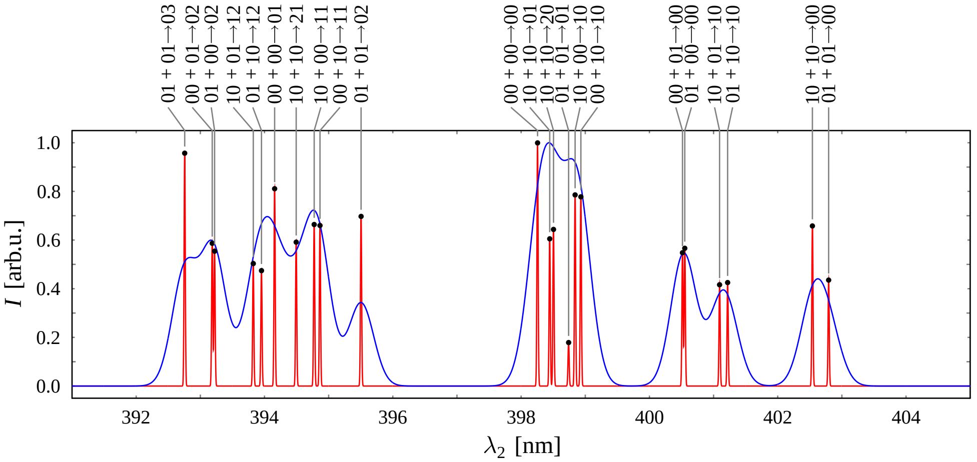

Fig. 8. Theoretical SH spectral intensity I observed in an ideal (red curve) and real (blue curve) structure. Individual combinations of spatial modes are identified.

spectrum is relatively broad (see Fig. 8). As SH spectra belonging to individual processes are relatively wide and close to each other, only spectral filtering of the SH field itself is not sufficient to distinguish them. After spectral filtering, individual processes become experimentally available by exciting only specific spatial modes in the fundamental beam. Technically, the proper excitation of the chosen spatial mode(s) is accomplished by suitable coupling of the pump beam into the waveguide.

Modes (TE + TM → TE)	$\lambda_{2,\mathrm{exp}}$ [nm]	$\lambda_{2,\mathrm{theor}}$ [nm]	$\Delta\lambda_{2,\mathrm{exp}}$ [nm]	P_{exp} [arb.u.]	P_{theor} [arb.u.]
00 + 00 → 00	398.3	398.6	0.8	1.00	1.00
00 + 00 → 01	394.2	394.4	0.9	0.65	0.81
10 + 00 → 10	398.8	399.5	0.6	0.42	0.78
01 + 01 → 00	402.8	403.0	0.8	0.38	0.43
10 + 01 → 10	401.1	401.9	0.9	0.35	0.42
01 + 01 → 01	398.7	397.1	0.6	0.32	0.18

Table 2. Individual SHG processes identified in the waveguide, experimental central SH wavelength $\lambda_{2,\mathrm{exp}}$, theoretical central SH wavelength $\lambda_{2,\mathrm{theor}}$, spectral width $\Delta\lambda_{2,\mathrm{exp}}$, experimental relative power P_{exp}, and theoretical relative power P_{theor} are given. Experimental central wavelengths are measured with the error 0.1 nm given by the spectrometer response function. Spectral widths (relative powers) have the relative error 5% (9%).

Careful alignment of the pump-beam coupling and use of 3 nm wide spectral filters in this beam have allowed to observe cca 10 spectral lines from the SH spectrum plotted in Fig. 8. SH central wavelengths λ_2, spectral widths $\Delta\lambda_2$ as well as relative powers of the observed SHG processes are summarized in Table 2. The comparison of theoretical and experimental parameters in Table 2 has revealed good agreement in central wavelengths of the SH lines. Larger differences between the theoretical and experimental relative powers P can be explained by the difficulties in reaching an efficient coupling of the corresponding pump mode. The experimental spatial intensity profiles of the three interacting modes and the corresponding SH intensity spectra are plotted in Fig. 7 for three typical mode combinations. These graphs document real capabilities in controlling spatial properties of the SH beam. If the analyzed waveguide were used for parametric down-conversion, several individual processes based on different spatial modes would simultaneously occur contributing together to the signal and idler fields' profiles [e.g., parametric processes (0,0) → (0,0) + (0,0) and (0,0) → (0,1) + (0,1)]. This might be used for the generation of modally entangled photon pairs [32]. We finally note that temperature tuning is important in the determination of efficient individual processes. This gives additional possibilities in controlling the properties of the generated fields.

6. Conclusions

The process of second harmonic generation in a periodically-poled KTP waveguide has been investigated both experimentally and theoretically. Three types of the nonlinear processes (type II, I, and 0) have been observed simultaneously utilizing the first, second and third harmonics of the spatial nonlinear modulation. A scalar finite elements method based on the Galerkin method has been applied to calculate spatial mode profiles, propagation constants, and frequencies of the interacting fields. It has been shown that positions of the spectral lines of individual processes depend strongly on waveguide's depth and width in ideal waveguides. In real waveguides, fabrication imperfections considerably broaden single spectral lines occurring in ideal waveguides. Individual spatial and spectral processes in type II interaction have been experimentally characterized by changing pump-beam spectral filtering and coupling into the waveguide. The analyzed waveguide has been recognized as a versatile source of second-harmonic light.

Acknowledgements

Support by the project IAA100100713 of GA AS CR is acknowledged. The authors gratefully acknowledge the support by the Operational Program Research and Development for Innovations - European Regional Development Fund project CZ.1.05/2.1.00/03.0058 and project COST OC09026 of the Ministry of Education. R.M. acknowledges the support by the project PrF_2012_003 of Palacký University. J.Sv. thanks the project FI-DGR 2011 of The Catalan Government. R.M. and J.Sv. also gratefully acknowledge the support by the Operational Program Education for Competitiveness - European Social Fund (project CZ.1.07/2.3.00/20.0017 of the Ministry of Education).